

# Nonlinear magic: multiphoton microscopy in the biosciences

Warren R Zipfel, Rebecca M Williams & Watt W Webb

Multiphoton microscopy (MPM) has found a niche in the world of biological imaging as the best noninvasive means of fluorescence microscopy in tissue explants and living animals. Coupled with transgenic mouse models of disease and 'smart' genetically encoded fluorescent indicators, its use is now increasing exponentially. Properly applied, it is capable of measuring calcium transients 500  $\mu\text{m}$  deep in a mouse brain, or quantifying blood flow by imaging shadows of blood cells as they race through capillaries. With the multitude of possibilities afforded by variations of nonlinear optics and localized photochemistry, it is possible to image collagen fibrils directly within tissue through nonlinear scattering, or release caged compounds in sub-femtoliter volumes.

MPM is a form of laser-scanning microscopy that uses localized 'nonlinear' excitation to excite fluorescence only within a thin raster-scanned plane and nowhere else. Since its first demonstration by our group over a decade ago<sup>1</sup>, MPM has been applied to a variety of imaging tasks and has now become **the technique of choice for fluorescence microscopy in thick tissue and in live animals**. Neuroscientists have used it to measure calcium dynamics deep in brain slices<sup>2–11</sup> and in live animals<sup>12–14</sup> (reviewed in ref. 15), to study neuronal plasticity<sup>16</sup> and to monitor neurodegenerative disease models in brain slices<sup>17</sup> and in living mice<sup>18–21</sup>. MPM has proved invaluable to cancer researchers for *in vivo* studies of angiogenesis<sup>22,23</sup> and metastasis<sup>24,25</sup>, to immunologists for investigating lymphocyte trafficking<sup>26–30</sup> and to embryologists for visualizing a day in the life of a developing hamster embryo<sup>31</sup>. **These types of applications define the most important niche for MPM—high-resolution imaging of physiology, morphology and cell-cell interactions in intact tissues or live animals.**

Although two-photon excited fluorescence is usually the primary signal source in MPM, three-photon excited fluorescence<sup>32–37</sup> and second-<sup>37–45</sup> and third-harmonic generation (SHG, THG)<sup>46–48</sup> can also be used for imaging. In fact, SHG imaging was one of the earliest forms of biological nonlinear microscopy, proposed<sup>49</sup> and demonstrated<sup>38</sup> decades ago. Notably, one of the most complex forms of nonlinear imaging, coherent anti-Stokes Raman scattering (CARS) microscopy, was developed even earlier<sup>50</sup>. CARS microscopy derives contrast directly from Raman-active vibrational modes within molecules and requires two synchronized pulsed lasers operating at different wavelengths, rather than a single pulsed laser as in two- (or three)-photon and SHG and THG microscopy. Like SHG microscopy, CARS microscopy lay dormant for decades but has recently been markedly improved<sup>51,52</sup> with the help of tunable, pulsed lasers in the infrared (IR) wavelength range.

Nonlinear excitation also has 'nonimaging' uses in biological research, such as the three-dimensional photolysis of caged molecules in femtoliter volumes<sup>16,53–56</sup>, diffusion measurements by multiphoton fluorescence correlation spectroscopy (MP-FCS)<sup>57,58</sup> and multiphoton fluorescence photobleaching recovery (MP-FPR or MP-FRAP)<sup>16,59–61</sup>, and detecting bimolecular interactions using multiphoton two-color cross-correlation spectroscopy (MP-FCCS)<sup>62</sup>. Targeted, localized multiphoton excitation has also been used for transfection of single cells by opening a transient nanoscopic pore in the cell membrane with a parked femtosecond laser<sup>63</sup>. Precise ablation and cutting is possible on the subcellular level. For example, a small region from a single chromosome from a fixed cell can be excised<sup>64</sup>, opening the possibility of sub-chromosomal ablation in a living cell to study the effect of knocking out specific regions of a targeted chromosome.

Here, we review applications of MPM and provide a simplified, practical view of the optical, technological and photophysical aspects of this type of microscopy that may be foreign to biologists but is fundamental to an understanding of how best to apply this technology.

## Moore's law of multiphoton microscopy

A search of publications referencing MPM (and its various synonyms) reveals several facts about the integration of this relatively new imaging technology into biological research. Publications involving MPM have increased exponentially over the past decade (Fig. 1) as femtosecond laser sources became robust and commercially available, and as the first commercial multiphoton microscopes were introduced in 1996 by BioRad Microscience (Hemel Hempstead, UK). About half of the total references have been consistently devoted to technique and instrumentation development rather than focused on specific biological questions. This is at least partly attributable to the unexplored potential of nonlinear optical processes for biological research (pointed out as early as 1978; ref. 49).

A survey of the instrumentation used in the studies employing MPM for biological research (255 out of 560 total references) indicates that 66% of these studies made use of laboratory-built systems, usually based

School of Applied and Engineering Physics, 212 Clark Hall, Cornell University, Ithaca, New York 14853, USA. Correspondence should be addressed to W.W.W. ([www2@cornell.edu](mailto:www2@cornell.edu)).

Published online 31 October 2002; doi:10.1038/nbt899

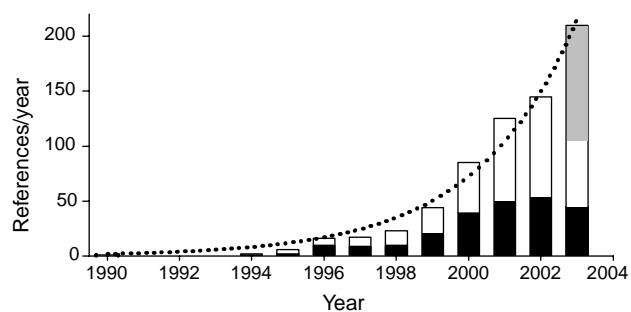


**Figure 1** Publications employing, developing or reviewing MPM (from PubMed and ISI). Bar height (white and black) indicates the total number of references for the given year; black bars represent publications focusing on instrumentation development, the remainder being work in which MPM was used to help clarify a specific biological research goal. Gray bar is the estimated number based on twice the 2003 half-year total; dotted line is an exponential fit of the data.

on modified confocal microscopes. The remaining one-third employed commercial systems—27% from BioRad and 3.5% each from Zeiss (Oberkochen, Germany) and Leica (Wetzlar, Germany). Furthermore, the majority (~80%) of the publications are from a small number of research groups (~12) who have developed the required expertise to use the technique effectively. Taken together, these statistics indicate that MPM is still a specialized technology, used successfully by some, but apparently not yet at the level of routine use characteristic of conventional (single-photon) confocal microscopy.

### Three-dimensionally localized excitation

Early in the development of quantum mechanics, it was shown theoretically by Maria Göppert-Mayer<sup>65</sup> that photons of lesser energy together can cause an excitation 'normally' produced by the absorption of a single photon of higher energy in a process called multiphoton or two-photon excitation. Two-photon microscopy, as normally practiced, uses the simplest version of her theoretical prediction: two photons of about equal energy (from the same laser) interact with a molecule, producing an excitation equivalent to the absorption of a single photon possessing twice the energy. If the excited molecule is fluorescent, it can emit a single photon of fluorescence as if it were excited by a single higher energy photon (Fig. 2). This event depends on the two photons both interacting with the molecule nearly simultaneously (~10<sup>-16</sup> s), resulting in a quadratic dependence on the light intensity rather than the linear dependence of conventional fluorescence. Multiphoton processes such as two-photon excitation (TPE) are often termed 'nonlinear' because the rate at which they occur depends nonlinearly on the intensity. The intensity-squared dependence is the basis of the localized nature of two-photon excitation: doubling the intensity produces four times the fluorescence.

In MPM, as in conventional laser-scanning confocal microscopy, a laser is focused and raster-scanned across the sample. The image consists of a matrix of fluorescence intensity measurements made by digitizing the detector signal as the laser sweeps back and forth across the sample. TPE probabilities are extremely small, and focusing increases the local intensity at the focal point. Intensity ( $I$ ) is the number of photons passing through a unit area per unit time (usually in photons cm<sup>-2</sup> s<sup>-1</sup>), whereas power is energy per second (1 W = 1 J s<sup>-1</sup>). Because intensity depends on the area, it is greater at the focus than a distance away, whereas the total power is the same everywhere along the beam. To calculate the intensity from measured laser power readings, 1 mW =  $\lambda \times 5 \times 10^{12}$  photons s<sup>-1</sup> nm<sup>-1</sup> can be used (derived from  $E = hc/\lambda$ ). For example, 1 mW at 960 nm is  $\sim 5 \times 10^{15}$  photons s<sup>-1</sup>.

Dividing this by the area of the beam in the focal plane (for high numerical aperture (NA)  $\sim 10^{-9}$  cm<sup>2</sup>) gives an intensity at the focus of  $\sim 5 \times 10^{24}$  photons cm<sup>-2</sup> s<sup>-1</sup>. The intensity squared is  $25 \times 10^{48}$  photons<sup>2</sup> cm<sup>-4</sup> s<sup>-2</sup>, increasing the TPE probability in the focal plane by  $\sim 10^7$  compared with the unfocused beam. Away from the focal plane, the TPE probability drops off rapidly so that no appreciable fluorescence is emitted (Fig. 2b), and intrinsic three-dimensional resolution is achieved.

Focusing alone is still not enough to make two-photon microscopy practical. For example, 1 mW of 960-nm light focused into 10  $\mu$ m fluorescein generates only  $\sim 20,000$  fluorescence photons per second. Further reduced by a total collection efficiency of only a few percent, this intensity would be much less than one fluorescence photon per pixel on a typical laser-scanning microscope with a  $\sim 1$ - $\mu$ s pixel dwell time. To generate enough TPE fluorescence for imaging, a pulsed laser is used to increase further the probability that two photons will simultaneously interact with a molecule, while still keeping the *average* power relatively low. A mode-locked titanium sapphire (Ti:S) laser—the most common laser used in MPM—produces  $\sim 80$  million pulses per second, each with pulse duration of  $\sim 100$  fs. With a pulsed laser, the two-photon fluorescence depends on the *average squared intensity* ( $\langle I(t)^2 \rangle$ ) rather than the *squared average intensity* ( $\langle I(t) \rangle^2$ ). The average intensity is equal to the number of pulses per second ( $R$ ) times the integrated instantaneous intensity during a pulse, which yields<sup>36,66</sup>

$$\langle I(t)^2 \rangle = g_p \langle I(t) \rangle^2 / (R\tau) \quad (1)$$

where  $g_p$  is a unitless factor that depends on the temporal laser pulse shape (0.66 for a Gaussian pulse shape),  $\tau$  is the full-width half-maximum (FWHM) of the pulse and  $\langle \rangle$  denotes the time-averaged value. For 100-fs pulses and  $R = 80$  MHz, the TPE probability is increased by  $g_p/R\tau \approx 10^5$ , and 20,000 emitted photons becomes 2 billion photons per second with a mode-locked laser. This translates into around 100 photons per pixel in the imaginary multiphoton microscope just described.

### Fluorescence excitation and two-photon action cross-sections

The two-photon cross-section ( $\sigma_{2p}$ ) is a quantitative measure of the probability of a two-photon absorption.  $\sigma_{2p}$  has units of cm<sup>4</sup> s, with 10<sup>-50</sup> cm<sup>4</sup> s called a Göppert-Mayer or 'GM'. Because it is difficult to measure  $\sigma_{2p}$  directly, the two-photon 'action' cross-section is usually measured; this is the product of the fluorescence quantum yield ( $\phi_F$ ) and the absolute two-photon absorption cross-section ( $\sigma_{2p}$ )<sup>36,66,67</sup>. Both the wavelength dependence and the absolute values of  $\phi_F\sigma_{2p}$  are important

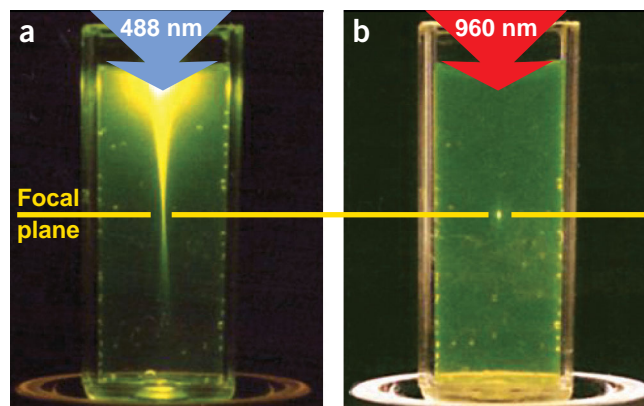


**Figure 2** Localization of excitation by two-photon excitation. (a) Single-photon excitation of fluorescein by focused 488-nm light (0.16 NA). (b) Two-photon excitation using focused (0.16 NA) femtosecond pulses of 960-nm light.

in MPM. To determine an optimal TPE wavelength, doubling the maximum single-photon excitation wavelength is often a good approximation. However, many molecules exhibit obvious deviations from this rule because the selection rules for two-photon processes are different from single-photon selection rules. For symmetrical molecules, initial single-photon excited states are two-photon forbidden<sup>68</sup>, and therefore fluorophores such as Rhodamine B<sup>67</sup> show a clear difference between their one- and two-photon absorption spectra, as shown in Figure 3a.

Intrinsic molecules such as NADH have extremely low action cross-sections ( $<10^{-4}$  GM)<sup>36,37,69</sup> yet have been successfully used with MPM imaging<sup>70–73</sup>. The other extreme, CdSe-ZnS quantum dots, have cross-sections approaching 50,000 GM<sup>74</sup> and allow multiphoton imaging with a few microwatts of laser power. Most common fluorescent dyes have  $\phi_F\sigma_{2p}$  values in the range of 1–300 GM<sup>36,67</sup>, although it is possible to design organic molecules specifically for high nonlinear absorption<sup>75–77</sup>. Intrinsically fluorescent proteins, such as green fluorescent protein (GFP), have large action cross-sections (Fig. 3b and refs. 36, 78–81), and are particularly well suited for MPM in tissue explants and live animals<sup>24,82–88</sup>.

Although relative two-photon excitation spectra ( $\lambda$  dependence)<sup>89,90</sup> can be useful, it is often necessary to know  $\phi_F\sigma_{2p}(\lambda)$  explicitly when designing a particular MPM experiment. For example, cyan fluorescent protein (CFP) and yellow fluorescent protein (YFP) can be used for multiphoton fluorescence resonance energy transfer (MP-FRET)<sup>91–93</sup> but also have potential for MP-FCCS<sup>62</sup>. For MP-FRET, CFP must be excited without exciting YFP; for MP-FCCS, by contrast, it is optimal to excite both proteins equally. The relative excitation spectra alone do not provide the needed information, and an absolute measure of the expected fluorescence from each species at a given wavelength is necessary. From Figure 3c, it is clear that **MP-FRET is best carried out at 800 nm, whereas MP-FCCS would work best where the fluorescence from both species is about equal (~910 nm).**

### The optical and effective resolution of MPM

The optical resolution of a multiphoton microscope seems at first thought to be worse by a factor of 2 than a single-photon confocal microscope, because the illumination used is about twice the wavelength. However, this assessment is based on comparison to a hypothetical perfect confocal microscope that has an infinitely small pinhole<sup>94</sup>. As the pinhole is opened, the resolution of a confocal microscope decreases and the resolution difference becomes less. In practice, the effective resolution achieved is a function of many complex factors, such as the absolute number of photons collected per pixel (pixel noise scales as the square root of the number of photons), and, in a confocal microscope, the fraction of true signal photons relative to scattered photons from outside the observation volume (that is, contrast). Because fluorescence only arises from the focus in MPM, when compared with confocal in scattering samples the effective resolution of the former often seems far superior<sup>95–97</sup>.

Knowing the dimensions of the two-photon focal volume is useful, for example, to estimate the thickness of an optical section or to calculate the number of caged neurotransmitters one might expect to photolyse per laser pulse. The illumination point spread function,  $\text{IPSF}(x,y,z)$ , describes intensity everywhere in space near the focus, and in MPM only  $\text{IPSF}^2$  is needed to define the true optical resolution<sup>98</sup> (assuming confocal detection is not used).  $\text{IPSF}^2$  can be calculated (Fig. 4a) based on the work of Richards and Wolf<sup>99</sup>, and fits of the lateral and axial intensity-squared profiles to a Gaussian function (Fig. 4b) yield expressions for estimating the diffraction-limited lateral ( $\omega_{xy}$ ) and axial ( $\omega_z$ )  $1/e$  radii of  $\text{IPSF}^2$  (Fig. 4c). For NAs  $\leq 0.7$ ,  $\omega_{xy}$  is inversely proportional to NA; however, at higher NAs, this dependence deviates, and a better estimate

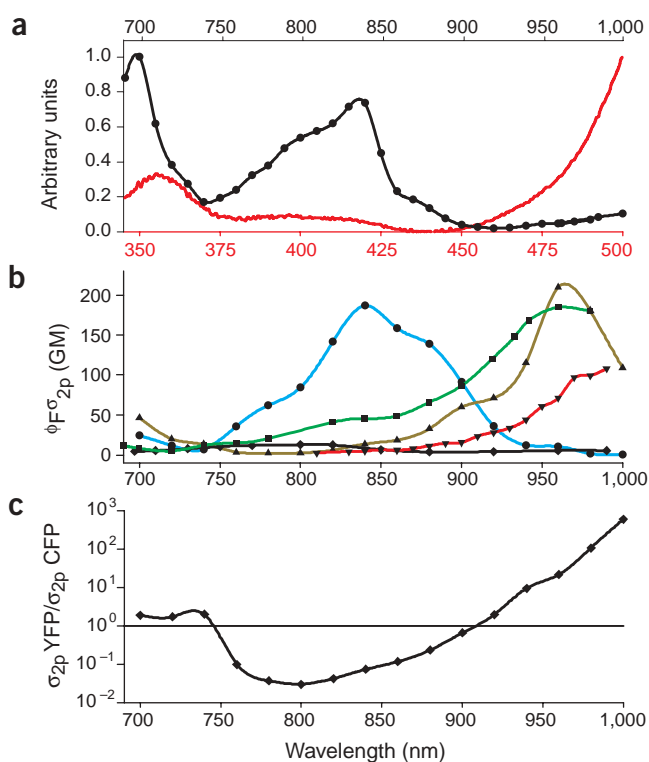


**Figure 3** Two-photon action cross-sections. (a) Two-photon action spectrum of Rhodamine B (black) compared to the one-photon absorption spectrum (red). (b) Two-photon action spectra of five common fluorescent proteins (FPs): enhanced GFP (eGFP; green), CFP (cyan), YFP (yellow), *Discosoma* Red (dsRed; red) and wild type GFP (wtGFP; black). Note: our measurements of the FP cross-sections were normalized to the concentration of fluorescing protein as determined by FCS, and therefore our absolute values (but not line shape) for CFP and YFP differ from refs. 79 and 81. (c) Semilog plot of the cross-section ratio of YFP to CFP.

(~1% error) can be found by assuming a slight inverse power dependence of NA. Analogous to the nonparaxial derivations of ref. 100, an expression for  $\omega_z$  of the two-photon focal volume can also be formulated (Fig. 4c). Conversions to the FWHM and  $1/e^2$  radius (Fig. 4b) can be obtained by multiplication by  $2\sqrt{\ln 2}$  and  $\sqrt{2}$ , respectively. The FWHM is a more common measure of optical resolution, whereas the  $1/e^2$  radius is, for example, needed to recover diffusion coefficients from MP-FCS and MP-FPR measurements. Note that the objective lenses must be uniformly illuminated (overfilled) to achieve a diffraction-limited focus—a condition well approximated if, in practice, the  $1/e$  beam diameter is no less than the diameter of the objective lens back aperture.

By approximating the  $\text{IPSF}^2$  as a three-dimensional Gaussian volume, analytical integration over all space yields the TPE focal volume. This is not a volume with distinct walls but rather one based on averaging the TPE potential over all space. Integrating the three-dimensional Gaussian yields

$$V_{\text{TPE}} = \pi^{3/2} \omega_{xy}^2 \omega_z \quad (2)$$

where  $\omega_{xy}$  and  $\omega_z$  are calculated as in Figure 4c. Although these expressions provide a good estimate of the central lobe of  $\text{IPSF}^2$ , they do not fully take the wings of  $\text{IPSF}^2$  into account at regions far from the focus and the integrated Gaussian volume yields a value 68% of that obtained from numerical integration of the full vectorial approach of ref. 99. With

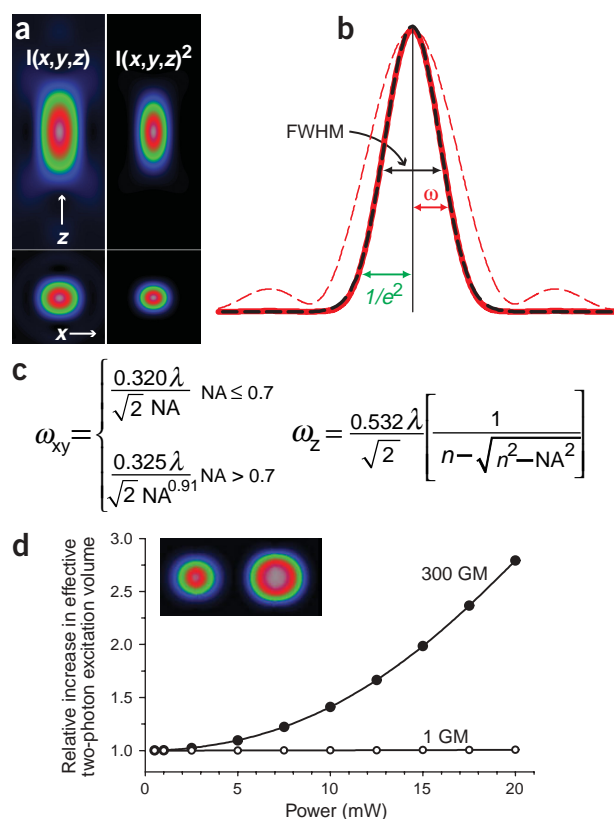


**Figure 4** The two-photon excitation volume. (a) Axial and lateral views of IPSPF and IPSPF<sup>2</sup>. Squaring the IPSPF results in minimal wings relative to the center. (b) Axial profile (0,0,z) of IPSPF (dashed red line) and IPSPF<sup>2</sup>(0,0,z) (solid red). Dashed black line is a fit to a Gaussian function. (c) Equations for calculating the 1/e widths ( $\omega$ ) of the lateral (xy) and axial (z) intensity-squared profiles. (d) Excitation probability saturation of the TPE focal volume for a 1-GM and 300-GM fluorophore calculated at 1.2 NA for a 200-fs, 80-MHz source. Insert shows the lateral plane of the effective IPSPF<sup>2</sup> at the focus for 1 GM (left) and 300 GM (right) at 20 mW.

this correction, equation (2) provides a good estimate of the TPE volume. For example, the effective TPE volume for a 1.2-NA lens at 900 nm is (5.57) (0.175  $\mu\text{m}$ )<sup>2</sup> (0.451  $\mu\text{m}$ ) / 0.68 = 0.113  $\mu\text{m}^3$  or ~100 attoliters.

In using a Gaussian approximation for the focal volume, it is assumed that the laser intensity is far from a level that would cause fluorophore excitation saturation. Assuming the lifetime of a fluorophore is less than the time between laser pulses, the TPE probability per laser pulse per fluorophore is  $1 - \exp(-\alpha\sigma_{2p}P^2\text{IPSPF}^2(x,y,z)/(R^2\tau))$ , where P is the laser power and  $\alpha$  is a conversion constant<sup>174</sup>. Depending on the laser power and the value of  $\sigma_{2p}$ , this probability can saturate near the focal center (*i.e.*, become 1.0), while continuing to increase in the wings of the focal volume, resulting in a marked deviation from the excitation volume predicted by equation (2). **Figure 4d** shows calculations carried out for molecules with cross-sections of 1 and 300 GM for laser powers up to 20 mW ( $R = 80$  MHz and 1.2 NA), indicating that with a relatively high cross-section dye the optical resolution may begin to deviate from the optimal possible value. This effect was clearly seen with quantum dots<sup>74</sup>, which have extremely high TPE cross sections. It also may become significant in cases where the peak laser intensity is unusually high, such as in applications of high-pulse power regenerative amplifier systems<sup>101,102</sup> to increase imaging depth. Similar calculations carried out with  $R = 200$  KHz for only 0.5 mW of power at the

focus yield an effective TPE volume 40 times larger than the nonsaturated focal volume.

### Lasers and laser optics for MPM

The application of mode-locked Ti:S crystal-based lasers to MPM, first demonstrated in 1992 (ref. 103), was really the beginning of practical MPM. Before that, MPM involved femtosecond dye lasers, which were temperamental and required constant tweaking. Commercial Ti:S lasers from Spectra-Physics (Mountain View, CA, USA) and Coherent (Sunnyvale, CA), now with broadband optics permitting use of the full tunable range (~700 to 1,000 nm) without changing laser mirrors, have made MPM an accessible tool for biology. The recent introduction of computer-controlled, single-box Ti:S lasers from both companies continues this trend. Although other types of mode-locked lasers have been applied<sup>31,95,104,105</sup>, Ti:S lasers are presently the most common and robust excitation sources for MPM.

The term ‘mode-locked’ refers to a laser operating with only a certain set of frequencies (modes) propagating in the laser cavity, with the phase between these modes locked so that there is destructive interference between the propagating frequencies everywhere in the cavity except at one point where the waves add constructively<sup>106</sup>. This results in a single short pulse of light traveling in the cavity with the repetition rate dictated by the distance between the two cavity end mirrors and the speed of light (**Fig. 5a,b**). Femtosecond Ti:S lasers require a relatively large number of intracavity frequencies to achieve 100-fs pulses, and therefore the pulses have a significantly large spectral bandwidth. The laser spectrum is simpler to measure than the pulsewidth, so it is commonly monitored in a MPM system as an indication of proper mode-locking. The spectrum should be a symmetrical Gaussian shape (**Fig. 5c**) devoid of spikes that indicate an unwanted continuous-wave component (termed ‘CW breakthrough’). The product of the pulsewidth and the spectral width (bandwidth) is called the time-bandwidth product (TBWP), which has a defined minimum value (the actual value depends on the temporal pulse shape). If the TBWP is equal to this minimum value, the pulses are ‘transform-limited’ and, assuming a Gaussian pulse shape, the temporal and spectral widths are related by  $\tau = 0.44\lambda_0^2/c \lambda_{\text{FWHM}}$ , where  $\lambda_0$  is the peak of the spectrum (that is, 960 nm in **Fig. 5c**) and  $c = 300$  nm/fs (speed of light). In a transform-limited pulse the wavelengths are randomized so any available color is equally probable anytime during the pulse. However, if this pulse passes through a dispersive material such as glass, it becomes ‘chirped’; the longer wavelength components travel faster so the pulsewidth lengthens, but the spectrum remains unchanged. In the visible and near-IR region, all materials have positive dispersion (red leads blue), so that femtosecond pulses passing through optics are always ‘positively chirped’ and thus longer than they were directly out of the laser. Positive dispersion can be offset by adding negative dispersion before the beam travels through the optics. This is known as dispersion compensation, or pre-chirping, and has been applied to MPM<sup>107,108</sup> but leads to an instrument that is more complicated to operate.

From equation (1) it can be shown that the increase in average power needed to maintain the same TPE with the longer pulse scales as the square root of the ratio of the chirped pulsewidth to the pulsewidth before the dispersive optics. For example, 2-fold increases in pulsewidth require 1.41-fold more laser power to achieve the same level of fluorescence. Pulse broadening resulting from dispersion can be estimated using

$$\tau_{\text{out}} = \tau_{\text{in}} (1 + 7.68(D/\tau_{\text{in}}^2)^2)^{1/2} \quad (3)$$

where  $D$  is the total dispersion in femtoseconds squared. A typical MPM system can have between 3,000 and 20,000 fs<sup>2</sup> of dispersion in

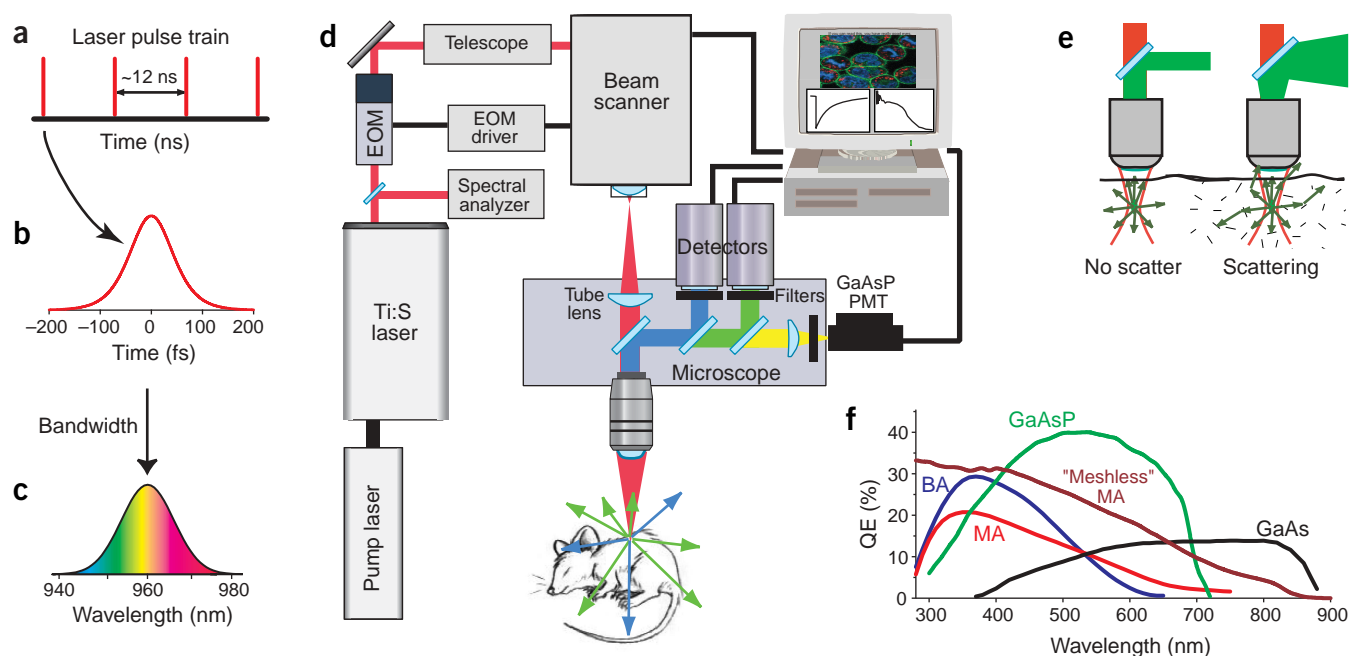


**Figure 5** Components of a multiphoton microscope. (a) Pulse train from a laser mode-locked Ti:S at 80 MHz. (b) Pulses out of the laser typically have a FWHM duration of 100 fs and a spectral FWHM (c) of  $\sim 10$  nm. (d) Schematic of a MPM system (see text). (e) Rays generated at the focus deep in a specimen may be scattered and enter the objective lens as skew rays, resulting in diverging epifluorescence. (f) Comparison of PMT photocathode efficiencies.

total, depending on the operating wavelength, objective lens used<sup>109–111</sup> and other components such as beam modulators and beam-expanding lenses. Laser pulsewidths vary as well, typically ranging from 80 to 150 fs, depending on the manufacturer and wavelength. At 5,000 fs<sup>2</sup>, this translates into pulsewidths of 190 and 177 fs, respectively, with both values being well within the range for efficient TPE. For a more dispersive system at 20,000 fs<sup>2</sup>, the respective pulsewidths become 697 fs and 403 fs, requiring 50–80% more average power to have the same TPE efficiency as the  $\sim 180$ -fs pulses available at the focus of the less dispersive system.

### The complete multiphoton microscope

Most multiphoton microscopes, including all commercial versions, essentially consist of a laser-scanning confocal adapted to reflect the near IR, a pulsed laser and a few required multiphoton peripherals. **Figure 5d** diagrams the components of a functional MPM system, similar to instruments reported in the literature<sup>112,113</sup>.

**Ti:S laser.** A choice exists between a pair of two separate lasers (Nd:YVO<sub>4</sub> pump laser and Ti:S laser) or a 'single-box' version, which has both the pump laser and Ti:S oscillator in the same factory-sealed box. The two-laser combination presently has a broader tuning range than a single-box laser (as much as 690–1,020 nm compared with 720–920 nm) and the ability to stop mode-locking, which is sometimes useful to verify that the signal is actually due to two-photon fluorescence. Laser power available varies depending on the size of the pump laser, with 5 W pumped systems providing up to 1 W at the Ti:S peak wavelengths ( $\sim 800$  nm) and a few hundred milliwatts near the edges of the tuning curve (700 nm and 1,000 nm). Systems with a 10 W pump source produce  $\sim 50\%$  more power across the wavelength range. For maximum flexibility and tuning range, the pump laser–Ti:S pair is as yet unsurpassed; however, simplicity of operation makes single-box lasers ideal for many situations, such as imaging facilities at which user friendliness is a priority.

**Beam intensity control.** There are several choices for controlling the laser intensity: a collection of neutral-density (ND) filters, a rotatable polarizer, an electro-optic modulator (EOM or Pockels cell) or an acousto-optic modulator (AOM). The two modulators have the ability to blank the beam during scanner turnaround and flyback; however, EOMs are typically less dispersive. For example, an EOM with a 50- to 80-mm-long KD\*P crystal has between 2,000 and 4,000 fs<sup>2</sup> of dispersion, whereas an AOM made of TeO<sub>2</sub> can be 4-fold more dispersive<sup>114</sup>.

**Beam telescope.** A beam telescope can be used to adjust the size of the beam at the back aperture of the objective to be sure the lens is 'over-filled' for a diffraction-limited focus, or in some cases, underfilled for an axially extended focus. Note that in the position shown in **Figure 5d**, the range of useable beam diameters is ultimately limited by the size of the XY scanner mirrors, which may be only a few millimeters in diameter. With the availability of the new high-NA, low-magnification objectives, such as the Olympus 20  $\times$  0.95 NA water immersion lens, which has a 17-mm back aperture, a better solution may be necessary. For example, beam expansion after the scanner is more optically complex to incorporate, but could better provide the range of beam sizes needed to optimize the focus.

**Beam scanner.** Of the various XY scanner designs available<sup>115</sup>, the most common is the nonresonant point scanner, which scans the focused beam across the specimen with an adjustable scan speed, permitting software 'zooming' (variable apparent magnification by scanning a smaller region, more slowly) and the important ability to rotate the scan axis. Resonant galvanometers capable of faster (video) scan rates<sup>116,117</sup> can also be used, but these operate at only one frequency and cannot zoom, pan or rotate. Also useful is the ability to park the beam stably at any specified XY position, allowing point measurements such as MP-FCS<sup>58</sup> and MP-FPR measurements<sup>59</sup> using the same optics for both imaging and single-point measurements. This is critical for intracellular measurements<sup>60</sup> so that the measurement location is accurately known.

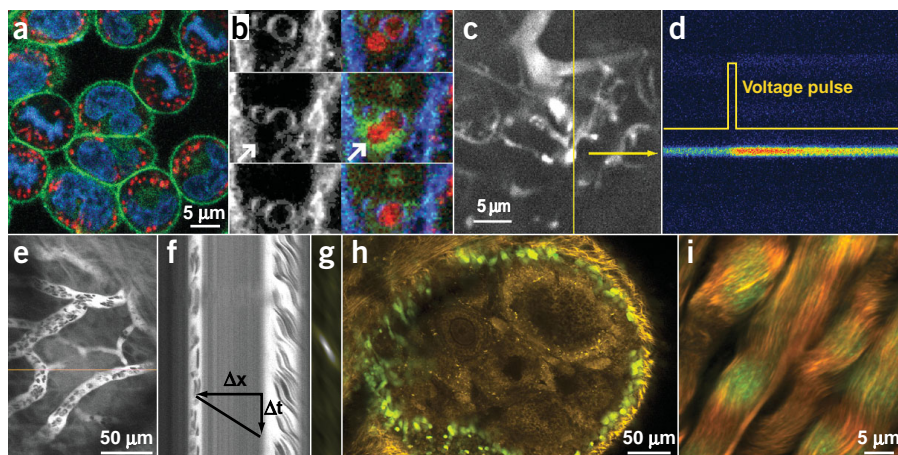


**Figure 6** Applications showing various capabilities of MPM. (a) Simultaneous 780-nm excitation of three different fluorophores in RBL-2H3 cells labeled with 4',6-diamidino-2-phenylindole (DAPI) (DNA, blue pseudo color), PATMAN (plasma membrane, green) and tetramethylrhodamine (mitochondria, red). (b) Cell stimulation-induced granule-granule fusion<sup>142</sup>, as assessed by PATMAN membrane staining (gray scale and blue) and acridine orange-stained granules (green and red). (c) and (d) Calcium dynamics 300  $\mu\text{m}$  deep into the neuropil of the lobster stomatogastric ganglion<sup>143</sup>. (e) Processes of a 'PD' neuron filled with calcium green-1N. (d) A line scan shows that upon depolarization (pulse), in a dopamine-dependent manner, calcium enters through varicosities on the neurites, copyright 2000 (reprinted by permission of the Society for Neuroscience, ©2000) (e) Measuring blood flow in a vessel plexus under the intact tibial growth plate perichondrium in the mouse. Red blood cells appear as shadows within the fluorescence-containing blood vessels (methodology from ref. 144, and work carried out in collaboration with C. Farnum, Cornell University, and W. Horton, Shriners' Hospital, Portland, Oregon). (f) The angle of the shadow traces in the line scan can be translated to the blood flow velocity. (g) Two-dimensional image autocorrelation is used to determine the average angle, in this case yielding an average blood flow of  $\Delta x/\Delta t = 226 \mu\text{m s}^{-1}$ . (h) Intrinsic emissions (yellow) detailing the tissue structure of a mouse's ovary can be imaged simultaneously with genetically incorporated GFPs. Ovarian surface epithelial cells were labeled by an intrabursal injection of virally incorporated eGFP. (Work done in collaboration with A. Flesken-Nikitin and A. Nikitin, Cornell University.) (i) Because collagen SHG is coherent, information about the specimen can be derived from the directionality of the SHG emission. In this 10-day-old rat tail tendon, immature fibril segments scatter backward (green), whereas mature fibrils scatter forward (red).

**Detectors.** The most efficient fluorescence collection scheme is obtained by the use of 'non-descanned' or direct detectors, because confocal detection is not needed with multiphoton excitation. Although it has been shown that a confocal aperture can improve the resolution of a two-photon microscope under certain conditions<sup>94,118</sup>, for applications in which MPM is most advantageous (such as deep imaging in scattering specimens) a confocal pinhole will degrade performance because scattered emission photons will be rejected, even though they originated in the focal volume. In fact, highly scattered emissions may even be randomly divergent leaving the objective lens (Fig. 5e) and thus difficult to focus<sup>101,119</sup>. For this reason, a particularly efficient detector design involves the use of a large-area photomultiplier tubes (PMT) close to the objective lens.

PMTs are the dominant detectors for both confocal and MPM because an imaging detector is not needed for point-scanning systems, and the high gain and absence of readout noise favors PMTs (pixel integration times are usually in the microsecond range). Charge-coupled detectors (CCDs) have not found widespread use in MPM, other than in situations requiring imaging detectors<sup>120</sup>, but are rapidly improving with on-chip avalanche amplification to reduce the effect of readout noise. Avalanche photodiodes (APDs) have also been used in MPM and may be superior to conventional PMTs at extremely low fluorescence levels<sup>121</sup>.

A recent improvement in detectors for MPM are GaAsP photocathode PMTs (Hamamatsu H7422P), which offer high quantum efficiency

(QE) values in the important 400- to 650-nm range compared with PMTs using conventional photocathode materials (Fig. 5f). Peaking at ~42% QE, GaAsP detectors are close to the theoretical 50% maximum QE of a photocathode-based device, making them well suited for two-photon FCS, as well as multiphoton imaging. They also have a small transient-time spread (~150 ps) and a 1-ns output pulse, making them attractive for fluorescence lifetime imaging<sup>122</sup>. Two minor limitations are a relatively small active area of 5 mm diameter (this is, however, still much larger than an APD active area), making focusing optics a requirement, and a lower damage threshold than conventional photocathodes. Overall, they are a significant advancement in MPM detectors because higher detection efficiency can translate to lower excitation power and improved viability with live specimens. For wavelengths beyond 700 nm, GaAs PMTs can be used, in addition to enhanced 'meshless' multialkali PMTs (such as the Hamamatsu H7732-10), which have a relatively high QE, even above 650 nm (Fig. 5f).

#### Applications of MPM

The advantages of MPM, for the most part, arise from two basic attributes of the nonlinear excitation: localized excitation and the expanded wavelength accessibility of most fluorophores. The restriction of multiphoton excitation to the focal plane completely alleviates out-of-focus photobleaching and photodamage. All photons generated are signal; there is no background, so that emission collection can be both simple and efficient. The

lack of out-of-focus fluorescence, coupled with the use of IR light, explains the technique's successful use for fluorescence imaging in thick specimens. The second aspect, enhanced UV bands under TPE (Fig. 3a), simplifies multicolor imaging by allowing excitation of different fluorophores with the same laser, avoiding chromatic aberrations and providing a broad uninterrupted emission collection bandwidth.

Figure 6 shows a panorama of applications that highlight the strengths of MPM, including the simultaneous excitation of fluorophores whose emission spectra vary by hundreds of nanometers (Fig. 6a,b), deep imaging in live preparations (Fig. 6c,d) and live mice (Fig. 6e-h), as well as the use of intrinsic fluorophores and other nonlinear signals, such as SHG (Fig. 6h,i).

In addition to multiphoton fluorescence, an MPM system can easily be modified to collect light from nonlinear scattering processes, such as SHG. In harmonic generation, multiple photons simultaneously interact with non-centrosymmetrical structures without absorption, producing radiation at exactly half of the exciting wavelength (Fig. 7a). Because harmonic generation is a coherent process (scattered photons maintain phase information), the scattered beam must satisfy phase-matching constraints producing highly directed radiation rather than isotropic emission (Fig. 7b,c). SHG directionality is dependent on the distribution and directionality of the induced dipoles within the focal volume<sup>40,123</sup>. SHG imaging is presently being investigated to image membrane potential sensing dyes with improved signal-to-

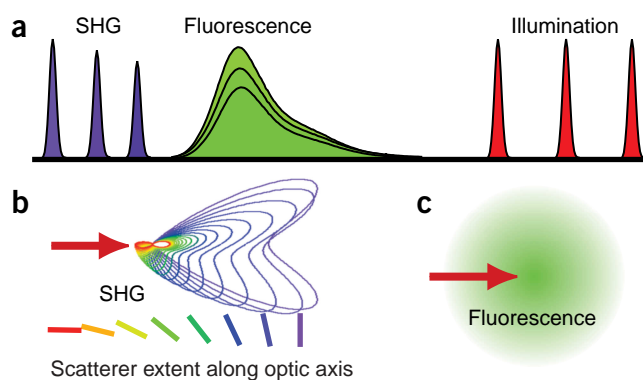


**Figure 7** Two-photon fluorescence and SHG. (a) SHG is always at half the fundamental wavelength and tunes with laser, whereas fluorescence emission is unchanged, except in its magnitude as the laser tunes through the TPE absorption peak. (b,c) SHG is directional depending on the distribution and orientation of the nonlinear dipoles (b), whereas fluorescence is, in general, isotropically emitted (c).

noise<sup>39,124–126</sup>, to visualize microtubule polarity<sup>42,44,127</sup> and to obtain high-resolution images of unstained collagen structures in mouse models of disease<sup>24,37,127</sup>.

#### Viability, photodamage and photobleaching

Although multiphoton excitation limits photodamage to the focal plane, the possibility of bleaching and damage within this region remains. Photodamage and decreased viability may be especially pronounced at the shorter Ti:S wavelengths where TPE of intrinsic tissue chromophores<sup>37</sup> is high. Clear enhancements in cellular viability with MPM over single-photon confocal microscopy are easiest to obtain at wavelengths  $>800$  nm<sup>31,128</sup>. It is generally thought that overall in the 700- to 1,000-nm range, single- and three-photon excitation damage is usually negligible, and photodamage in the focal plane is primarily due to two-photon processes<sup>129</sup>, implying that pulsewidth is usually not a critical parameter in viability. This finding is contradicted by work that suggests highly nonlinear dependence of phototoxicity<sup>130</sup>; however, the excitation doses (squared power  $\times$  dwell time) used in the work were nearly 1,000-fold higher than levels normally used in MPM. Probe photobleaching, like cellular photodamage, can only occur in the focal plane, but there is evidence that some molecules bleach more easily under TPE<sup>131</sup> and may even show higher order ( $>2$ ) photobleaching<sup>132</sup>.

Nonetheless, reduced damage outside of the focal volume can have tremendous advantages in optically thick specimens. The key to using MPM safely and successfully is not any different from that for any other form of microscopy; one must understand the effects and limits on the specific biological system under investigation, and always optimize to reduce the excitation intensity. In MPM, this means using efficient fluorescence detectors and blanking the laser while image data are not being acquired.

#### Conclusions and future areas of development

MPM is quickly becoming a standard tool for determining the molecular mechanisms of cell-based processes in basic biological research, tissue engineering and transgenic mouse models of disease and development. The number of publications focused on nonlinear microscopy development indicates that MPM has created its own field of research. Areas of development that hold particular promise range from fabrication of minimally dispersive objective lenses designed to optimize collection of scattered emissions, to the application of adaptive

optics<sup>133–135</sup> to MPM for correcting aberrations of the point spread function.

As presently implemented, MPM can image hundreds of microns deep. We believe the ultimate depth limitation is not often a result of a lack of laser power but rather difficulty in collecting the generated fluorescence due to both absorption and scattering, which leads to collection losses (Fig. 5e), as well as reduced fluorescence due to degradation of the IPSPF<sup>2</sup>. A simple test for inadequate two-photon excitation is to measure the power dependence of the fluorescence deep within the specimen to test for saturation. If it scales as less than the power squared, saturation is occurring, indicating that more than sufficient excitation exists in the focal plane. In practice, we often find blurriness and a significant reduction in contrast in many specimens when the imaging depth is increased past several hundred microns, well before all signal is lost. Aberrations of IPSPF<sup>2</sup> can be caused by either heterogeneity in the index of refraction in tissue or TPE focal volume saturation (see Fig. 4d). It may be possible to overcome the former difficulty by adaptive optics, in which the spatial phase of the beam is modified to pre-compensate for the path the rays take through the tissue. Curing the latter problem requires lower power, compensated by better detection.

Nonlinear optics, the ‘magical’ area of modern physics that helped spawn MPM, still has more to offer. Femtosecond lasers are being devised that can operate in the 1,000- to 1,300-nm range, just beyond that which a Ti:S laser can conveniently reach<sup>136,137</sup>. This region is especially important for high-viability imaging of redder dyes and fluorescent proteins. Several groups are developing forms of multiphoton endoscopy<sup>138,139</sup>, and new photonic crystal fibers now allow fiber delivery of 100-fs pulses through optical fibers with more than enough power for MPM and multiphoton endoscopy<sup>140</sup>. Finally, the trick of modifying nonlinear optical responses by changing the phase of the spectral components that make up a femtosecond pulse—a field known as ‘coherent control’—may make it possible to fine-tune multiphoton excitation<sup>141</sup> to increase multiphoton absorption, reduce two-photon photobleaching or improve photo-uncaging efficiency.

Since its introduction a little over a decade ago, MPM has evolved from a photonic novelty to a tool for visualizing cellular and subcellular events within living tissue. As we focus on understanding the physiological and developmental consequences of the multitude of new genetic sequences uncovered, but not understood, MPM will surely continue to play an important part.

#### COMPETING INTERESTS STATEMENT

The authors declare competing financial interests (see the *Nature Biotechnology* website for details).

Published online at <http://www.nature.com/naturebiotechnology/>

- Denk, W., Strickler, J.H. & Webb, W.W. Two-photon laser scanning fluorescence microscopy. *Science* **248**, 73–76 (1990).
- Yuste, R. & Denk, W. Dendritic spines as basic functional units of neuronal integration. *Nature* **375**, 682–684 (1995).
- Mainen, Z.F., Malinow, R. & Svoboda, K. Synaptic calcium transients in single spines indicate that NMDA receptors are not saturated. *Nature* **399**, 151–155 (1999).
- Rose, C.R., Kovalchuk, Y., Eilers, J. & Konnerth, A. Two-photon Na<sup>+</sup> imaging in spines and fine dendrites of central neurons. *Pflügers Arch.* **439**, 201–207 (1999).
- Tan, Y.P. & Llano, I. Modulation by K<sup>+</sup> channels of action potential-evoked intracellular Ca<sup>2+</sup> concentration rises in rat cerebellar basket cell axons. *J. Physiol.* **520 Pt 1**, 65–78 (1999).
- Cox, C.L., Denk, W., Tank, D.W. & Svoboda, K. Action potentials reliably invade axonal arbors of rat neocortical neurons. *Proc. Natl. Acad. Sci. USA* **97**, 9724–9728 (2000).
- Majewska, A., Tashiro, A. & Yuste, R. Regulation of spine calcium dynamics by rapid spine motility. *J. Neurosci.* **20**, 8262–8268 (2000).
- Oertner, T.G. Functional imaging of single synapses in brain slices. *Exp. Physiol.* **87**, 733–736 (2002).
- Frick, A., Magee, J., Koester, H.J., Migliore, M. & Johnston, D. Normalization of Ca<sup>2+</sup> signals by small oblique dendrites of CA1 pyramidal neurons. *J. Neurosci.* **23**, 3243–3250 (2003).
- Lendvai, B., Zelles, T., Rozsa, B. & Vizi, E.S. A vinca alkaloid enhances morphological

- dynamics of dendritic spines of neocortical layer 2/3 pyramidal cells. *Brain Res. Bull.* **59**, 257–260 (2003).
11. Sabatini, B.L. & Svoboda, K. Analysis of calcium channels in single spines using optical fluctuation analysis. *Nature* **408**, 589–593 (2000).
  12. Svoboda, K., Denk, W., Kleinfeld, D. & Tank, D.W. *In vivo* dendritic calcium dynamics in neocortical pyramidal neurons. *Nature* **385**, 161–165 (1997).
  13. Helmchen, F., Svoboda, K., Denk, W. & Tank, D.W. *In vivo* dendritic calcium dynamics in deep-layer cortical pyramidal neurons. *Nat. Neurosci.* **2**, 989–996 (1999).
  14. Stosiek, C., Garaschuk, O., Holthoff, K. & Konnerth, A. *In vivo* two-photon calcium imaging of neuronal networks. *Proc. Natl. Acad. Sci. USA* **100**, 7319–7324 (2003).
  15. Helmchen, F. & Waters, J. Ca(2+) imaging in the mammalian brain *in vivo*. *Eur. J. Pharmacol.* **447**, 119–129 (2002).
  16. Svoboda, K., Tank, D.W. & Denk, W. Direct measurement of coupling between dendritic spines and shafts. *Science* **272**, 716–719 (1996).
  17. Ladewig, T. *et al.* Spatial profiles of store-dependent calcium release in motoneurons of the nucleus hypoglossus from newborn mouse. *J. Physiol.* **547**, 775–787 (2003).
  18. Christie, R.H. *et al.* Growth arrest of individual senile plaques in a model of Alzheimer's disease observed by *in vivo* multiphoton microscopy. *J. Neurosci.* **21**, 858–864 (2001).
  19. Bacskai, B.J. *et al.* Non-Fc-mediated mechanisms are involved in clearance of amyloid-beta *in vivo* by immunotherapy. *J. Neurosci.* **22**, 7873–7878 (2002).
  20. D'Amore, J.D. *et al.* *In vivo* multiphoton imaging of a transgenic mouse model of Alzheimer disease reveals marked thioflavine-S-associated alterations in neurite trajectories. *J. Neuropathol. Exp. Neurol.* **62**, 137–145 (2003).
  21. Bacskai, B.J. *et al.* Imaging of amyloid-beta deposits in brains of living mice permits direct observation of clearance of plaques with immunotherapy. *Nat. Med.* **7**, 369–372 (2001).
  22. Brown, E.B. *et al.* *In vivo* measurement of gene expression, angiogenesis and physiological function in tumors using multiphoton laser scanning microscopy. *Nat. Med.* **7**, 864–868 (2001).
  23. McDonald, D.M. & Choyke, P.L. Imaging of angiogenesis: from microscope to clinic. *Nat. Med.* **9**, 713–725 (2003).
  24. Wang, W. *et al.* Single cell behavior in metastatic primary mammary tumors correlated with gene expression patterns revealed by molecular profiling. *Cancer Res.* **62**, 6278–6288 (2002).
  25. Wolf, K. *et al.* Compensation mechanism in tumor cell migration: mesenchymal-amoeboid transition after blocking of pericellular proteolysis. *J. Cell Biol.* **160**, 267–277 (2003).
  26. Cahalan, M.D., Parker, I., Wei, S.H. & Miller, M.J. Two-photon tissue imaging: seeing the immune system in a fresh light. *Nat. Rev. Immunol.* **2**, 872–880 (2002).
  27. Miller, M.J., Wei, S.H., Parker, I. & Cahalan, M.D. Two-photon imaging of lymphocyte motility and antigen response in intact lymph node. *Science* **296**, 1869–1873 (2002).
  28. Wei, S.H., Miller, M.J., Cahalan, M.D. & Parker, I. Two-photon imaging in intact lymphoid tissue. *Adv. Exp. Med. Biol.* **512**, 203–208 (2002).
  29. Miller, M.J., Wei, S.H., Cahalan, M.D. & Parker, I. Autonomous T cell trafficking examined *in vivo* with intravital two-photon microscopy. *Proc. Natl. Acad. Sci. USA* **100**, 2604–2609 (2003).
  30. Acuto, O. T cell–dendritic cell interaction *in vivo*: random encounters favor development of long-lasting ties. *Science STKE* **2003**, PE28 (2003).
  31. Squirrell, J.M., Wokosin, D.L., White, J.G. & Bavister, B.D. Long-term two-photon fluorescence imaging of mammalian embryos without compromising viability. *Nat. Biotechnol.* **17**, 763–767 (1999).
  32. Gryczynski, I., Szmajdzinski, H. & Lakowicz, J.R. On the possibility of calcium imaging using Indo-1 with three-photon excitation. *Photochem. Photobiol.* **62**, 804–808 (1995).
  33. Lakowicz, J.R. *et al.* Time-resolved fluorescence spectroscopy and imaging of DNA labeled with DAPI and Hoechst 33342 using three-photon excitation. *Biophys. J.* **72**, 567–578 (1997).
  34. Maiti, S., Shear, J.B., Williams, R.M., Zipfel, W.R. & Webb, W.W. Measuring serotonin distribution in live cells with three-photon excitation. *Science* **275**, 530–532 (1997).
  35. Williams, R.M., Shear, J.B., Zipfel, W.R., Maiti, S. & Webb, W.W. Mucosal mast cell secretion processes imaged using three-photon microscopy of 5-hydroxytryptamine autofluorescence. *Biophys. J.* **76**, 1835–1846 (1999).
  36. Xu, C., Zipfel, W., Shear, J.B., Williams, R.M. & Webb, W.W. Multiphoton fluorescence excitation: new spectral windows for biological nonlinear microscopy. *Proc. Natl. Acad. Sci. USA* **93**, 10763–10768 (1996).
  37. Zipfel, W.R. *et al.* Live tissue intrinsic emission microscopy using multiphoton-excited native fluorescence and second harmonic generation. *Proc. Natl. Acad. Sci. USA* **100**, 7075–7080 (2003).
  38. Freund, I. & Deutsch, M. 2<sup>nd</sup>-harmonic microscopy of biological tissue. *Opt. Lett.* **11**, 94–96 (1986).
  39. Campagnola, P.J., Clark, H.A., Mohler, W.A., Lewis, A. & Loew, L.M. Second-harmonic imaging microscopy of living cells. *J. Biomed. Opt.* **6**, 277–286 (2001).
  40. Mertz, J. & Moreaux, L. Second-harmonic generation by focused excitation of inhomogeneously distributed scatterers. *Opt. Commun.* **196**, 325–330 (2001).
  41. Moreaux, L., Sandre, O., Charpak, S., Blanchard-Desce, M. & Mertz, J. Coherent scattering in multi-harmonic light microscopy. *Biophys. J.* **80**, 1568–1574 (2001).
  42. Campagnola, P.J. *et al.* Three-dimensional high-resolution second-harmonic generation imaging of endogenous structural proteins in biological tissues. *Biophys. J.* **82**, 493–508 (2002).
  43. Campagnola, P.J., Mohler, W. & Millard, A.E. 3-dimensional high-resolution second harmonic generation imaging of endogenous structural proteins in biological tissues. *Biophys. J.* **82**, 175a–175a (2002).
  44. Dombbeck, D.A. *et al.* Uniform polarity microtubule assemblies imaged in native brain tissue by second-harmonic generation microscopy. *Proc. Natl. Acad. Sci. USA* **100**, 7081–7086 (2003).
  45. Zoumi, A., Yeh, A. & Tromberg, B.J. Imaging cells and extracellular matrix *in vivo* by using second-harmonic generation and two-photon excited fluorescence. *Proc. Natl. Acad. Sci. USA* **99**, 11014–11019 (2002).
  46. Barad, Y., Eisenberg, H., Horowitz, M. & Silberberg, Y. Nonlinear scanning laser microscopy by third harmonic generation. *Appl. Phys. Lett.* **70**, 922–924 (1997).
  47. Muller, M., Squier, J., Wilson, K.R. & Brakenhoff, G.J. 3D microscopy of transparent objects using third-harmonic generation. *J. Microsc.* **191**, 266–274 (1998).
  48. Yelin, D., Oron, D., Korkotian, E., Segal, M. & Silberberg, Y. Third-harmonic microscopy with a titanium-sapphire laser. *Appl. Phys. B—Lasers O* **74**, S97–S101 (2002).
  49. Sheppard, C.J.R. & Kompfner, R. Resonant scanning optical microscope. *Appl. Optics* **17**, 2879–2882 (1978).
  50. Duncan, M.D., Reintjes, J. & Manuccia, T.J. Scanning coherent anti-Stokes Raman microscope. *Opt. Lett.* **7**, 350–352 (1982).
  51. Zumbusch, A., Holtom, G.R. & Xie, X.S. Vibrational microscopy using coherent anti-Stokes Raman scattering (1999). *Phys. Rev. Lett.* **82**, 4014–4017 (1999).
  52. Muller, M., Squier, J., De Lange, C.A. & Brakenhoff, G.J. CARS microscopy with folded BoxCARS phase-matching. *J. Microsc.* **197** (Pt 2), 150–158 (2000).
  53. Piston, D.W., Summers, R.G., Knobel, S.M. & Morrill, J.B. Characterization of involution during sea urchin gastrulation using two-photon excited photorelease and confocal microscopy. *Microsc. Microanal.* **4**, 404–414 (1998).
  54. Furuta, T. *et al.* Brominated 7-hydroxycoumarin-4-ylmethyls: photolabile protecting groups with biologically useful cross-sections for two-photon photolysis. *Proc. Natl. Acad. Sci. USA* **96**, 1193–1200 (1999).
  55. Matsuzaki, M. *et al.* Dendritic spine geometry is critical for AMPA receptor expression in hippocampal CA1 pyramidal neurons. *Nat. Neurosci.* **4**, 1086–1092 (2001).
  56. Echevarria, W., Leite, M.F., Guerra, M.T., Zipfel, W.R. & Nathanson, M.H. Regulation of calcium signals in the nucleus by a nucleoplasmic reticulum. *Nat. Cell. Biol.* **5**, 440–446 (2003).
  57. Berland, K.M., So, P.T. & Gratton, E. Two-photon fluorescence correlation spectroscopy: method and application to the intracellular environment. *Biophys. J.* **68**, 694–701 (1995).
  58. Schwiile, P., Haupts, U., Maiti, S. & Webb, W.W. Molecular dynamics in living cells observed by fluorescence correlation spectroscopy with one- and two-photon excitation. *Biophys. J.* **77**, 2251–2265 (1999).
  59. Brown, E.B., Wu, E.S., Zipfel, W. & Webb, W.W. Measurement of molecular diffusion in solution by multiphoton fluorescence photobleaching recovery. *Biophys. J.* **77**, 2837–2849 (1999).
  60. Zipfel, W.R. & Webb, W.W. *In vivo* diffusion measurements using multiphoton-excited fluorescence photobleaching recovery (MPFPR) and fluorescence correlation spectroscopy (MPFCS) in *Methods in Cellular Imaging* (ed. Periasamy, A.) 345–376 (Oxford University Press, Oxford, UK, 2001).
  61. Stroh, M., Zipfel, W.R., Williams, R.M., Webb, W.W. & Saltzman, W.M. Diffusion of nerve growth factor in rat striatum as determined by multiphoton microscopy. *Biophys. J.* **85**, 581–588 (2003).
  62. Heinze, K.G., Koltermann, A. & Schwiile, P. Simultaneous two-photon excitation of distinct labels for dual-color fluorescence cross correlation analysis. *Proc. Natl. Acad. Sci. USA* **97**, 10377–10382 (2000).
  63. Tirlapur, U.K. & Konig, K. Targeted transfection by femtosecond laser. *Nature* **418**, 290–291 (2002).
  64. Konig, K., Riemann, I. & Fritzsche, W. Nanodissection of human chromosomes with near-infrared femtosecond laser pulses. *Opt. Lett.* **26**, 819–821 (2001).
  65. Göppert-Mayer, M. Über elementarakt mit zwei quantensprüngen. *Ann. Phys.* **9**, 273–294 (1931).
  66. Xu, C. & Webb, W.W. Multiphoton excitation of molecular fluorophores and nonlinear laser microscopy in *Topics in Fluorescence Spectroscopy: Volume 5: Nonlinear and Two-Photon-Induced Fluorescence*. (ed. Lakowicz, J.) 471–540 (Plenum Press, New York, 1997).
  67. Xu, C. & Webb, W.W. Measurement of two-photon excitation cross sections of molecular fluorophores with data from 690 nm to 1050 nm. *J. Opt. Soc. Am. B* **13**, 481–491 (1996).
  68. Steinfeld, J.I. *Molecules and Radiation*. (MIT Press, Cambridge, MA, 1989).
  69. Huang, S., Heikal, A.A. & Webb, W.W. Two-photon fluorescence spectroscopy and microscopy of NAD(P)H and flavoprotein. *Biophys. J.* **82**, 2811–2825 (2002).
  70. Piston, D.W., Masters, B.R. & Webb, W.W. Three-dimensionally resolved NAD(P)H cellular metabolic redox imaging of the *in situ* cornea with two-photon excitation laser scanning microscopy. *J. Microsc.* **178** (Pt 1), 20–27 (1995).
  71. Wong, B.J., Wallace, V., Coleno, M., Benton, H.P. & Tromberg, B.J. Two-photon excitation laser scanning microscopy of human, porcine, and rabbit nasal septal cartilage. *Tissue Eng.* **7**, 599–606 (2001).
  72. Noda, M. *et al.* Switch to anaerobic glucose metabolism with NADH accumulation in the beta-cell model of mitochondrial diabetes. Characteristics of betaHC9 cells deficient in mitochondrial DNA transcription. *J. Biol. Chem.* **277**, 41817–41826 (2002).
  73. Zhang, Q., Piston, D.W. & Goodman, R.H. Regulation of corepressor function by nuclear NADH. *Science* **295**, 1895–1897 (2002).
  74. Larson, D.R. *et al.* Water-soluble quantum dots for multiphoton fluorescence imaging *in vivo*. *Science* **300**, 1434–1436 (2003).
  75. Albot, M. *et al.* Design of organic molecules with large two-photon absorption cross sections. *Science* **281**, 1653–1656 (1998).
  76. Wang, X.M. *et al.* Synthesis of new symmetrically substituted stilbenes with large multiphoton absorption cross section and strong two-photon-induced blue fluorescence. *Bull. Chem. Soc. Jpn* **74**, 1977–1982 (2001).
  77. Zhou, X. *et al.* One- and two-photon absorption properties of novel multi-branched molecules. *Phys. Chem. Chem. Phys.* **4**, 4346–4352 (2002).

78. Heikal, A.A., Hess, S.T. & Webb, W.W. Multiphoton molecular spectroscopy and excited-state dynamics of enhanced green fluorescent protein (EGFP): acid-base specificity. *Chem. Phys.* **274**, 37–55 (2001).
79. Blab, G.A., Lommerse, P.H.M., Cognet, L., Harms, G.S. & Schmidt, T. Two-photon excitation action cross-sections of the autofluorescent proteins. *Chem. Phys. Lett.* **350**, 71–77 (2001).
80. Hanson, G.T. *et al.* Green fluorescent protein variants as ratiometric dual emission pH sensors. 1. Structural characterization and preliminary application. *Biochemistry* **41**, 15477–15488 (2002).
81. Tsai, P.S. *et al.* All-optical histology using ultrashort laser pulses. *Neuron* **39**, 27–41 (2003).
82. Mainen, Z.F. *et al.* Two-photon imaging in living brain slices. *Methods* **18**, 231–239, (1999).
83. Shi, S.H. *et al.* Rapid spine delivery and redistribution of AMPA receptors after synaptic NMDA receptor activation. *Science* **284**, 1811–1816 (1999).
84. D'Apuzzo, M., Mandolesi, G., Reis, G. & Schuman, E.M. Abundant GFP expression and LTP in hippocampal acute slices by *in vivo* injection of Sindbis virus. *J. Neurophysiol.* **86**, 1037–1042 (2001).
85. Potter, S.M. *et al.* Structure and emergence of specific olfactory glomeruli in the mouse. *J. Neurosci.* **21**, 9713–9723 (2001).
86. Strome, S. *et al.* Spindle dynamics and the role of gamma-tubulin in early *Caenorhabditis elegans* embryos. *Mol. Biol. Cell* **12**, 1751–1764 (2001).
87. Ahmed, F. *et al.* GFP expression in the mammary gland for imaging of mammary tumor cells in transgenic mice. *Cancer Res.* **62**, 7166–7169 (2002).
88. Lawson, N.D. & Weinstein, B.M. *In vivo* imaging of embryonic vascular development using transgenic zebrafish. *Dev. Biol.* **248**, 307–318 (2002).
89. Bestvater, F. *et al.* Two-photon fluorescence absorption and emission spectra of dyes relevant for cell imaging. *J. Microsc.* **208**, 108–115 (2002).
90. Dickinson, M.E., Simburger, E., Zimmermann, B., Waters, C.W. & Fraser, S.E. Multiphoton excitation spectra in biological samples. *J. Biomed. Opt.* **8**, 329–338 (2003).
91. Periasamy, A. Fluorescence resonance energy transfer microscopy: a mini review. *J. Biomed. Opt.* **6**, 287–291 (2001).
92. Majoul, I., Straub, M., Duden, R., Hell, S.W. & Soling, H.D. Fluorescence resonance energy transfer analysis of protein-protein interactions in single living cells by multifocal multiphoton microscopy. *J. Biotechnol.* **82**, 267–277 (2002).
93. Bacskai, B.J., Koch, J., Hickey, G.A., Allen, R. & Hyman, B.T. Fluorescence resonance energy transfer determinations using multiphoton fluorescence lifetime imaging microscopy to characterize amyloid-beta plaques. *J. Biomed. Opt.* **8**, 368–375 (2003).
94. Gu, M. & Sheppard, C.J.R. Comparison of three-dimensional imaging properties between two-photon and single-photon fluorescence microscopy. *J. Microsc.* **177**, 128–137 (1995).
95. Centonze, V.E. & White, J.G. Multiphoton excitation provides optical sections from deeper within scattering specimens than confocal imaging. *Biophys. J.* **75**, 2015–2024 (1998).
96. Periasamy, A., Skoglund, P., Noakes, C. & Keller, R. An evaluation of two-photon excitation versus confocal and digital deconvolution fluorescence microscopy imaging in *Xenopus* morphogenesis. *Microsc. Res. Technol.* **47**, 172–181 (1999).
97. Schilders, S.P. & Gu, M. Limiting factors on image quality in imaging through turbid media under single-photon and two-photon excitation. *Microsc. Microanal.* **6**, 156–160 (2000).
98. Sheppard, C.J.R. & Gu, M. Image-formation in 2-photon fluorescence microscopy. *Optik* **86**, 104–106 (1990).
99. Richards, B. & Wolf, E. Electromagnetic Diffraction in Optical Systems. 2. Structure of the Image Field in an Aplanatic System. *Proc. R. Soc. Lon. Ser. -A* **253**, 358–379 (1959).
100. Sheppard, C.J.R. & Matthews, H.J. Imaging in high-aperture optical systems. *J. Opt. Soc. Am. A* **4**, 1354–1360 (1987).
101. Beaurepaire, E., Oheim, M. & Mertz, J. Ultra-deep two-photon fluorescence excitation in turbid media. *Opt. Commun.* **188**, 25–29 (2001).
102. Theer, P., Hasan, M.T. & Denk, W. Two-photon imaging to a depth of 1000 microm in living brains by use of a Ti:Al<sub>2</sub>O<sub>3</sub> regenerative amplifier. *Opt. Lett.* **28**, 1022–1024 (2003).
103. Curley, P.F., Ferguson, A.I., White, J.G. & Amos, W.B. Application of a femtosecond self-sustaining mode-locked Ti:sapphire laser to the field of laser scanning confocal microscopy. *Opt. Quant. Electron.* **24**, 851–859 (1992).
104. Hockberger, P.E. *et al.* Activation of flavin-containing oxidases underlies light-induced production of H<sub>2</sub>O<sub>2</sub> in mammalian cells. *Proc. Natl. Acad. Sci. USA* **96**, 6255–6260 (1999).
105. Wokosin, D.L., Squier, J.M., Eliceiri, K.W. & White, J.G. Optical workstation with concurrent, independent multiphoton imaging and experimental laser microbeam capabilities. *Rev. Sci. Instrum.* **74**, 193–201 (2003).
106. Hopkins, J. & Sibbett, W. Ultrashort lasers: big payoff in a flash. *Sci. Am.* **283**, 73–79 (2000).
107. Soeller, C. & Cannell, M.B. Construction of a two-photon microscope and optimization of illumination pulse duration. *Pflugers Arch.* **432**, 555–561 (1996).
108. Squier, J. & Muller, M. High resolution nonlinear microscopy: A review of sources and methods for achieving optimal imaging. *Rev. Sci. Instrum.* **72**, 2855–2867 (2001).
109. Muller, D., Squier, J. & Brakenhoff, G.J. Measurement of femtosecond pulses in the focal point of a high-numerical-aperture lens by two-photon absorption. *Opt. Lett.* **20**, 1038–1040 (1995).
110. Guild, J.B., Xu, C. & Webb, W.W. Measurement of group delay dispersion of high numerical aperture objective lenses using two-photon excited fluorescence. *Appl. Optics* **36**, 397–401 (1997).
111. Muller, M., Squier, J., Wolleschensky, R., Simon, U. & Brakenhoff, G.J. Dispersion compensation of 15 femtosecond optical pulses for high-numerical-aperture objectives. *J. Microsc.* **191**, 141–150 (1998).
112. Majewska, A., Yiu, G. & Yuste, R. A custom-made two-photon microscope and deconvolution system. *Pflugers Arch.* **441**, 398–408 (2000).
113. Tsai, P.S. *et al.* Principles, design and construction of a two-photon scanning microscope for *in vitro* and *in vivo* studies in *Methods for In Vivo Optical Imaging* (ed. Frostig, R.) 113–171 (CRC Press, Boca Raton, FL, 2002).
114. Iyer, V., Losavio, B.E. & Saggau, P. Compensation of spatial and temporal dispersion for acousto-optic multiphoton laser-scanning microscopy. *J. Biomed. Opt.* **8**, 460–471 (2003).
115. Pawley, J.B. *Handbook of Biological Confocal Microscopy*, edn 2. (Plenum Press, New York, 1995).
116. Fan, G.Y. *et al.* Video-rate scanning two-photon excitation fluorescence microscopy and ratio imaging with cameleons. *Biophys. J.* **76**, 2412–2420 (1999).
117. Nguyen, Q.T., Callamaras, N., Hsieh, C. & Parker, I. Construction of a two-photon microscope for video-rate Ca<sup>2+</sup> imaging. *Cell Calcium* **30**, 383–393 (2001).
118. Gauderon, R., Lukins, P.B. & Sheppard, C.J. Effect of a confocal pinhole in two-photon microscopy. *Microsc. Res. Technol.* **47**, 210–214 (1999).
119. Oheim, M., Beaurepaire, E., Chaigneau, E., Mertz, J. & Charpak, S. Two-photon microscopy in brain tissue: parameters influencing the imaging depth. *J. Neurosci. Methods* **111**, 29–37 (2001).
120. Egner, A., Jakobs, S. & Hell, S.W. Fast 100-nm resolution three-dimensional microscope reveals structural plasticity of mitochondria in live yeast. *Proc. Natl. Acad. Sci. USA* **99**, 3370–3375 (2002).
121. Tan, Y.P., Llano, I., Hopt, A., Wurriehausen, F. & Neher, E. Fast scanning and efficient photodetection in a simple two-photon microscope. *J. Neurosci. Methods* **92**, 123–135 (1999).
122. Gratton, E., Breusegem, S., Sutin, J., Ruan, Q. & Barry, N. Fluorescence lifetime imaging for the two-photon microscope: time-domain and frequency-domain methods. *J. Biomed. Opt.* **8**, 381–390 (2003).
123. Moreaux, L., Sandre, O. & Mertz, J. Membrane imaging by second-harmonic generation microscopy. *J. Opt. Soc. Am. B* **17**, 1685–1694 (2000).
124. Peleg, G., Lewis, A., Linial, M. & Loew, L.M. Nonlinear optical measurement of membrane potential around single molecules at selected cellular sites. *Proc. Natl. Acad. Sci. USA* **96**, 6700–6704 (1999).
125. Moreaux, L., Sandre, O., Blanchard-Desce, M. & Mertz, J. Membrane imaging by simultaneous second-harmonic generation and two-photon microscopy. *Opt. Lett.* **25**, 320–322 (2000).
126. Millard, A.C., Jin, L., Lewis, A. & Loew, L.M. Direct measurement of the voltage sensitivity of second-harmonic generation from a membrane dye in patch-clamped cells. *Opt. Lett.* **28**, 1221–1223 (2003).
127. Mohler, W., Millard, A.C. & Campagnola, P.J. Second harmonic generation imaging of endogenous structural proteins. *Methods* **29**, 97–109 (2003).
128. Konig, K., So, P.T., Mantulin, W.W., Tromberg, B.J. & Gratton, E. Two-photon excited lifetime imaging of autofluorescence in cells during UVA and NIR photostress. *J. Microsc.* **183** (Pt 3), 197–204 (1996).
129. Koester, H.J., Baur, D., Uhl, R. & Hell, S.W. Ca<sup>2+</sup> fluorescence imaging with pico- and femtosecond two-photon excitation: signal and photodamage. *Biophys. J.* **77**, 2226–2236 (1999).
130. Hopt, A. & Neher, E. Highly nonlinear photodamage in two-photon fluorescence microscopy. *Biophys. J.* **80**, 2029–2036 (2001).
131. Dittich, P.S. & Schwille, P. Photobleaching and stabilization of fluorophores used for single-molecule analysis with one- and two-photon excitation. *Appl. Phys. B: Lasers O* **73**, 829–837 (2001).
132. Patterson, G.H. & Piston, D.W. Photobleaching in two-photon excitation microscopy. *Biophys. J.* **78**, 2159–2162 (2000).
133. Neil, M.A. *et al.* Adaptive aberration correction in a two-photon microscope. *J. Microsc.* **200** (Pt 2), 105–108 (2000).
134. Booth, M.J., Neil, M.A. & Wilson, T. New modal wave-front sensor: application to adaptive confocal fluorescence microscopy and two-photon excitation fluorescence microscopy. *J. Opt. Soc. Am. A Opt. Image Sci. Vis.* **19**, 2112–2120 (2002).
135. Marsh, P.N., Burns, D. & Girkin, J.M. Practical implementation of adaptive optics in multiphoton microscopy. *Opt. Express* **11**, 1123–1130 (2003).
136. Brunner, F. *et al.* Diode-pumped femtosecond Yb:KGd(WO<sub>4</sub>/sub 4)/sub 2/ laser with 1.1-W average power. *Opt. Lett.* **25**, 1119–1121 (2000).
137. Ilday, F.O., Lim, H., Buckley, J.R. & Wise, F.W. Practical all-fiber source of high-power, 120-fs pulses at 1 micron. *Opt. Lett.* **28**, 1362–1364 (2003).
138. Jung, J.C. & Schmitzer, M.J. Multiphoton endoscopy. *Opt. Lett.* **28**, 902–904 (2003).
139. Bird, D. & Gu, M. Two-photon fluorescence endoscopy with a micro-optic scanning head. *Opt. Lett.* **28**, 1552–1554 (2003).
140. Ouzounov, D.G. *et al.* Delivery of nanosecond femtosecond pulses through large-core microstructured fibers. *Opt. Lett.* **27**, 1513–1515 (2002).
141. Pastirk, I., Dela Cruz, J.M., Walowicz, K.A., Lozovoy, V.V. & Dantus, M. Selective two-photon microscopy with shaped femtosecond pulses. *Opt. Express* **11**, 1695–1701 (2003).
142. Williams, R.M. & Webb, W.W. Single granule pH cycling in antigen-induced mast cell secretion. *J. Cell Sci.* **113** (Pt 21), 3839–3850 (2000).
143. Kloppenburg, P., Zipfel, W.R., Webb, W.W. & Harris-Warrick, R.M. Highly localized Ca<sup>2+</sup> accumulation revealed by multiphoton microscopy in an identified motoneuron and its modulation by dopamine. *J. Neurosci.* **20**, 2523–2533 (2000).
144. Kleinfeld, D., Mitra, P.P., Helmchen, F. & Denk, W. Fluctuations and stimulus-induced changes in blood flow observed in individual capillaries in layers 2 through 4 of rat neocortex. *Proc. Natl. Acad. Sci. USA* **95**, 15741–15746 (1998).